

Debris Object Orbit Initialization Using the Probabilistic Admissible Region with Asynchronous Heterogeneous Observations

Waqar H. Zaidi, Weston R. Faber, Islam I. Hussein, Michael Mercurio,
Christopher W. T. Roscoe, and Matthew P. Wilkins
Applied Defense Solutions

Paul W. Schumacher Jr.
United States Air Force Research Laboratory

ABSTRACT

One of the most challenging problems in treating space debris is the characterization of the orbit of a newly detected and uncorrelated measurement. The admissible region is defined as the set of physically acceptable orbits (i.e. orbits with negative energies) consistent with one or more measurements of a Resident Space Object (RSO). Given additional constraints on the orbital semi-major axis, eccentricity, etc., the admissible region can be constrained, resulting in the constrained admissible region (CAR). Based on known statistics of the measurement process, one can replace hard constraints with a Probabilistic Admissible Region (PAR), a concept introduced in 2014 as a Monte Carlo uncertainty representation approach using topocentric spherical coordinates. Ultimately, a PAR can be used to initialize a sequential Bayesian estimator and to prioritize orbital propagations in a multiple hypothesis tracking framework such as Finite Set Statistics (FISST). To date, measurements used to build the PAR have been collected concurrently and by the same sensor. In this paper, we allow measurements to have different time stamps. We also allow for non-located sensor collections; optical data can be collected by one sensor at a given time and radar data collected by another sensor located elsewhere. We then revisit first principles to link asynchronous optical and radar measurements using both the conservation of specific orbital energy and specific orbital angular momentum. The result from the proposed algorithm is an implicit-Bayesian and non-Gaussian representation of orbital state uncertainty.

1. INTRODUCTION

Spacecraft collision risk assessment between two space objects requires two key measures: their relative miss distance in an inertial frame of reference and the two objects' covariances at the time of closest approach (TCA). The covariance of a primary operational spacecraft in Low Earth Orbit (LEO) can remain Gaussian (in Cartesian elements) up to 10 days without the presence of drag.¹ As a result, the attention turns to tracking the second conjuncting object, most likely a piece of debris. This paper assumes the conjunction initially involves a piece of debris that belongs to a newly detected and uncorrelated measurement. Operating a spacecraft teaches us the probability of collision between well-tracked and sparsely tracked objects will remain elevated due to the covariance of the latter object, often leading to high intensity risk mitigation maneuver planning due to what is likely a false alarm, particularly if the Gaussianity of the covariance is misrepresented. Thus, we believe poor tracking of the secondary can be alleviated if methods are improved to obtain a non-uniform and non-Gaussian representation of the secondary object uncertainty, one that can initialize a sequential Bayesian estimator and lead to the faster convergence of a multiple hypothesis filter (MHF) such as FISST.²

The admissible region (AR), in the space surveillance field, is defined as the set of physically acceptable orbits (i.e. orbits with negative energies) consistent with one or more measurements of a RSO. Given additional constraints on the orbital elements a , e , etc., the admissible region can be constrained, resulting in the CAR. In previous work, Roscoe et al. extended this concept to include regions in the ρ - $\dot{\rho}$ plane satisfying orbital element bounds for pairs of measurements (the ρ - $\dot{\rho}$ admissible region) and investigated the effect of angle-rate uncertainty.^{3,4} Hussein et al. applied probabilistic techniques to obtain a non-uniform distribution of the points within the CAR using both unscented transform (UT) and Monte Carlo (MC) methods.⁵ This probabilistic form of the CAR would then be a PAR that itself can be expressed in one of two ways. The first version relies on a short-arc angles-only optical measurement, along with known measurement statistics as well as candidate a and e statistics resulting in a two-dimensional PAR, that is the probabilistic non-uniform distribution representation of the CAR. The second version relies on a sole angles-only optical measurement without rate information and incorporates known statistics in i and Ω to produce a

four-dimensional non-uniformly distributed generalized representation of the CAR. Both versions can be extended to a radar measurement with and without angle rate information, respectively.

In this study, we first focus on the sampling of a , e , i , and Ω to build a four-dimensional PAR. In our companion paper, the sampling bounds for these orbital elements were held tight to avoid particle depletion.⁶ This approach is feasible for an event such as a minor spacecraft breakup as we would know the prior probability density function (pdf) to sample around. This paper assumes there is no a priori information available for the uncorrelated track and it seeks to obtain the probabilistic representation of uncertainty by sampling orbital elements from the entire RSO catalog, albeit for the orbit regime being observed (i.e. LEO, MEO, or GEO). We note that opening the sampling bounds produces fewer PAR particles than before so we mitigate this depletion by either resampling the orbital elements (without replacement) that produced real particles or clustering existing solutions within the AR to produce a GMM representation of the PAR that can be randomly resampled to produce a denser representation of the pdf. Once the new pdf is obtained, we carry out the ensuing estimation updates at the time of a second asynchronous measurement.

Traditional Bayesian estimation requires characterizing a posterior pdf by fusing a predicted state pdf, determined via the Fokker-Planck-Kolmogorov equation (FPKE), with imperfect measurement data (the statistics of which are characterized by some Gaussian pdf). In the case of purely linear dynamical systems where all errors are characterized by Gaussian pdfs, the resulting posterior pdf is also Gaussian—a seminal result obtained by Kalman in 1960.⁷ For nonlinear dynamical systems, one may resort to linearization methods and Gaussian approximations to efficiently invoke a Bayesian update; thus, providing a Gaussian approximation for the posterior pdf.⁸ This paper revisits first principles of astrodynamics to maintain the non-uniformity of the PAR built at an initial time (using an uncorrelated optical measurement) that is updated with an optical or radar measurement sampled from the true orbit of the object later in its orbit (i.e. we are assuming data association between the two observations). The orbit dynamics between the times of both measurements are tied together using the conservation of specific orbital energy and specific orbital angular momentum^{*}; thus, no propagation is involved and instead an implicit-Bayesian update is performed using a Newton-Raphson solver to determine the radar or angular parameters (at the time of the second measurement). The result is a non-Gaussian representation of uncertainty, one that if propagated over an extended period should maintain high-order cumulants and provide a realistic search space for future measurement updates. The authors recognize non-conservative forces are ignored using conservation laws and have left the impact of doing so open for research.

This paper is divided into four main sections. The first section provides a review of the optical and radar probabilistic admissible regions. The second section describes the governing equations tying heterogeneous optical and radar measurements collected asynchronously; conservation equations are provided in terms of both optical and radar measurements. The third section provides a review of Bayesian estimation using an ensemble Kalman filter (EnKF). The last section provides two examples of a LEO PAR built using a single untracked and uncorrelated angles-only optical measurement that is updated with a second asynchronous (in time and collection) angles-only optical or radar measurement using the proposed implicit-Bayesian and traditional Bayesian approaches. In conclusion, uncertainty representations are compared between the two approaches.

2. PROBABILISTIC ADMISSIBLE REGION

The optical AR formed in this paper uses a spherical coordinate system known as the topocentric spherical system in which the orientation of the Earth J2000 axes is translated to a particle sensor location. The origin rotates with the Earth but maintains a fixed orientation at the sensor and the coordinates are given by the slant range vector ρ , topocentric right ascension α , and topocentric declination δ .[†] The position and velocity of a satellite expressed in topocentric spherical coordinates and the corresponding unit vectors in each direction are given by the following equations,

$$\mathbf{x} = [\alpha \ \delta \ \dot{\alpha} \ \dot{\delta} \ \rho \ \dot{\rho}]^T \quad (1)$$

$$\mathbf{u}_\rho = [\cos \alpha \cos \delta \ \sin \alpha \cos \delta \ \sin \delta]^T \quad (2)$$

$$\mathbf{u}_\alpha = [-\sin \alpha \ \cos \alpha \ 0]^T \quad (3)$$

$$\mathbf{u}_\delta = [-\cos \alpha \sin \delta \ -\sin \alpha \sin \delta \ \cos \delta]^T \quad (4)$$

^{*}Both specific orbital energy and specific angular momentum are designated as ‘orbital energy’ and ‘orbital angular momentum’ in the rest of this paper.

[†]The ‘ t ’ subscripts are dropped for the rest of this paper.

Farnocchia et al. describe the optical AR through a short-arc angles-only measurement represented by $[\alpha \ \delta \ \dot{\alpha} \ \dot{\delta}]^T$ and an inequality in the orbital energy to enclose possible trajectories of the observed object that solely orbit the Earth.⁹ More specifically, given a value for ϵ an AR represents curves corresponding to $\epsilon = 0$ inside which all orbits with negative energy ($\epsilon < 0$) exist. Essentially, the AR becomes a search space which can be used by a MHF to converge to the true location of the observed object with subsequent measurement updates. These maximum “semi-major axis constraints” are given by manipulating the two-body orbital energy expression in terms of the given measurement into inequalities that provide the boundaries of the optical AR,

$$\epsilon(\rho, \dot{\rho}) = \dot{\rho}^2 + \omega_1 \dot{\rho} + \omega_2 \rho^2 + \omega_3 \rho + \omega_4 - \frac{2\mu}{\sqrt{\rho^2 + \omega_5 \rho + \omega_0}} + \frac{u}{a_{max}} \leq 0 \quad (5)$$

Note the constants $\omega_1, \omega_2, \omega_3, \omega_4,$ and ω_5 are defined in the appendix.

The quantity $\|\mathbf{h}\|^2$ is related to e through the orbital energy as follows,

$$\epsilon = -\frac{\mu^2}{2\|\mathbf{h}\|^2} (1 - e^2) \quad (6)$$

Consequently, the optical AR is constrained further using an inequality in the relationship between $\|\mathbf{h}\|^2$ and e as follows,

$$\mathbf{h}(\rho, \dot{\rho}) = \mathbf{h}_1 \dot{\rho} + \mathbf{h}_2 \rho^2 + \mathbf{h}_3 \rho + \mathbf{h}_4 \quad (7)$$

Note the constants $h_1, h_2, h_3,$ and $h_4,$ are defined in the appendix.

Substituting Eq. [7] into Eq. [6] and then into Eq. [5] produces the following inequality or maximum “eccentricity” constraint for the optical AR,

$$a_4 \dot{\rho}^4 + a_3 \dot{\rho}^3 + a_2 \dot{\rho}^2 + a_1 \dot{\rho} + a_0 \leq 0 \quad (8)$$

Note the constants $a_0, a_1, a_2, a_3,$ and a_4 are defined in the appendix.

The size of the eccentricity constraint ellipse is dependent on the maximum sampled eccentricity. In fact, if one were to select a maximum eccentricity of say 0.9, the ellipse would encompass the entire semi-major axis constraint and all possible orbits would be constrained within the parabola. A plot of the optical AR is provided in Fig. [1]; given a range of ρ values, the a constraint curve represents the real $\dot{\rho}$ roots of Eq. [5] while the e constraint curve represents the real $\dot{\rho}$ roots of Eq. [8].

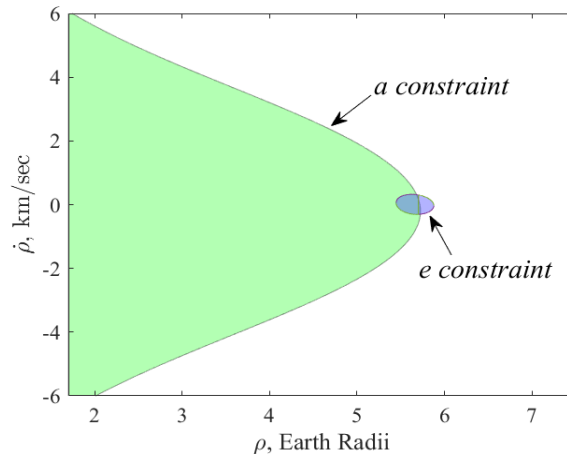


Figure 1. Optical Admissible Region.

Now that the AR of potential orbits for optical measurements is defined, the particle cloud representation of the PAR must be described in detail. The general goal is to obtain a probabilistic characterization of the uncertainty in the unknown variables $[\rho \ \dot{\rho}]^T$ given a short-arc angles-only measurement in $[\alpha \ \delta \ \dot{\alpha} \ \dot{\delta}]^T$. Specifically, four out of the six required orbital elements are available to completely characterize the orbit and the remaining two elements are completed using pdfs in $p(a)$ and $p(e)$. As a result, this version of the PAR receives a two-dimensional designation and the joint pdf in $[\alpha \ \delta \ \dot{\alpha} \ \dot{\delta} \ a \ e]^T$ is given by the following equation,

$$p(\alpha, \delta, \dot{\alpha}, \dot{\delta}, a, e) = p(\alpha, \delta, \dot{\alpha}, \dot{\delta})p(a)p(e) \quad (9)$$

Consequently, a and e are independent of the measurement and their distributions are sampled from a known population such as the public RSO catalog. When the number of available orbital elements are two instead of four, (i.e. a sole angles-only measurement), Ω and i are sampled in addition to a and e . The ensuing admissible region receives a four-dimensional designation and the joint pdf in $[\alpha \ \delta \ a \ e \ i \ \Omega]^T$ by the following equation,

$$p(\alpha, \delta, a, e, i, \Omega) = p(\alpha, \delta)p(a)p(e)p(i)p(\Omega) \quad (10)$$

The preceding uncertainty mapping is impossible to achieve in closed-form, even when the measurement process is Gaussian. This is due to the nonlinearity present in the preceding governing equations, rendering the uncertainty non-Gaussian, and thus allowing the usage of the MC method to obtain a particle representation of the uncertainty. Accordingly, Ref. [1] shows that one can map the left-hand sides of Eqs. [9] and [10] to obtain $p(\alpha, \delta, \dot{\alpha}, \dot{\delta}, \rho, \dot{\rho})$ when formulating the four-dimensional PAR using an angles-only measurement. It describes a procedure in which the sampled $[a \ e \ i \ \Omega]^T$ is used to construct the angular momentum vector in Eq. [11] that in turn gets set to the right-hand side of Eq. [7] to obtain Eq. [12] after rearranging terms,

$$\mathbf{h} = \mu a(1 - e^2) \begin{bmatrix} \sin i \sin \Omega \\ -\sin i \cos \Omega \\ \cos i \end{bmatrix} \quad (11)$$

$$\underbrace{\begin{bmatrix} c_1 \rho^2 + c_4 \rho & c_2 \rho^2 + c_5 \rho \end{bmatrix}}_A \underbrace{\begin{bmatrix} \dot{\alpha} \\ \dot{\delta} \end{bmatrix}}_x = \underbrace{\begin{bmatrix} h - c_3 \rho - h_4 - h_1 \rho \end{bmatrix}}_b \quad (12)$$

Note the constants $c_1, c_2, c_3, c_4,$ and c_5 are defined in the appendix.

At this point the authors note the system $Ax = b$ in Eq. (12) is over-determined as it contains 3 equations for 2 unknowns in $\dot{\alpha}$ and $\dot{\delta}$. We therefore resort to minimizing the L2 norm of the error by solving the linear system using the pseudo-inverse of the matrix A . Accordingly, given an angles-only measurement $[\alpha \ \delta]^T$ (for which there are the four unknowns in $\rho, \dot{\rho}, \dot{\alpha}, \dot{\delta}$), we only have three equations: one from Eq. [5] and two from Eq. [12]. Therefore, a fourth equation is needed and is available through the magnitude of the eccentricity vector,

$$\|\mathbf{e}\| = \frac{\|\dot{\mathbf{r}}\|^2 \mathbf{r}}{\mu} - \frac{(\mathbf{r} \cdot \dot{\mathbf{r}}) \mathbf{r}}{\mu} - \frac{\mathbf{r}}{\|\mathbf{r}\|} \quad (13)$$

A solution for the four-dimensional PAR exists when Eqs. [5], [12], and [13] are satisfied for a given value of $[\rho \ \dot{\rho}]^T$ and sampled set of $[a \ e \ i \ \Omega]^T$. However, the direction of the eccentricity vector remains ambiguous since the magnitude of the eccentricity vector was used to obtain $p(\alpha, \delta, \dot{\alpha}, \dot{\delta}, \rho, \dot{\rho})$. We can now state the attributable vector and the resulting AR for the two- and four-dimensional optical PAR case is summarized in Table 1.

Table 1. Two- and Four-Dimensional Attributable Vectors and Admissible Regions for Optical Sensors

Designation	Dimension	Attributable Vector	Range	Admissible Region
-------------	-----------	---------------------	-------	-------------------

Optical	2	$A_{opt} = (\alpha, \delta, \dot{\alpha}, \dot{\delta})$	$[0, 2\pi) \times (-\pi, \pi) \times \mathbb{R}^2$	$\{\rho, \dot{\rho}\}$
Optical	4	$A_{opt} = (\alpha, \delta)$	$[0, 2\pi) \times (-\pi, \pi)$	$\{\dot{\alpha}, \dot{\delta}, \rho, \dot{\rho}\}$

To generate a particle cloud representation of the four-dimensional optical PAR, it is assumed sensor noise characteristics as well as the statistics in $a, e, i,$ and Ω are given and the measurement process is Gaussian with means $[\mu^\alpha \ \mu^\delta]^\text{T}$ and covariances $[\Sigma^\alpha \ \Sigma^\delta]^\text{T}$ for right ascension and declination, respectively at a given time t . Given the measurement process is Gaussian, we can sample these distributions and generate a cloud of particles by solving Eqs. (5), (18), and (19). Specifically, let the particles in these variables be denoted by $\{(\alpha^{(j)}, \delta^{(j)})\}$, where $j = 1, \dots, N$, where N is the chosen number of particles to represent the uncertainty cloud. Note that by our assumption $a, e, i,$ and Ω are independent of the angles measurements, sampling of the angular variables can be done by directly sampling from $p(\alpha, \delta)$. Under the independence assumption, we can sample $p(a), p(e), p(i)$ and $p(\Omega)$ directly to obtain the particles $\{a^{(j)}\}, \{e^{(j)}\}, \{i^{(j)}\}$, and $\{\Omega^{(j)}\}, j = 1, \dots, N$, respectively. Notice that due to the statistical independence assumption, the ordering of the particles inside each of these particle sets is irrelevant, but each particle from each set has to be uniquely and consistently matched with one from each of the other sets to obtain joint particles $\{y^{(j)}\} = \{\alpha^{(j)}, \delta^{(j)}, a^{(j)}, e^{(j)}, i^{(j)}, \Omega^{(j)}\}, j = 1, \dots, N$.

Next, each particle $y^{(j)}$ can now be used in Eqs. (5), (18), and (19) to obtain particles $\{z^{(k)}\} = \{\dot{\alpha}^{(k)}, \dot{\delta}^{(k)}, \rho^{(k)}, \dot{\rho}^{(k)}\}, k = 1, \dots, M$, in angle-rates, range, range-rate space, where, in general, $M \neq N$. We note the mapping to $[\alpha \ \delta \ \rho \ \dot{\rho}]^\text{T}$ is not one-to-one since multiple solutions are possible for each particle $\{y^{(j)}\}$ due several factors: the $\dot{\rho}^2$ in Eq. (5), the ambiguity of the angular momentum vector in Eq. (18), and the ambiguity of the eccentricity vector in Eq. (19). In addition, a particle $\{y^{(j)}\}$ may not even have a real solution for $[\alpha \ \delta \ \rho \ \dot{\rho}]^\text{T}$ if the measurement sample is not compatible with the sampled orbital elements. The resulting set of $z^{(k)}$ particles is the desired particle cloud that represents the PAR.

3. SAMPLING FROM THE RESIDENT SPACE OBJECT CATALOG

Only the measurement statistics in $[\alpha \ \delta]^\text{T}$ are known for a four-dimensional PAR built using an angles-only uncorrelated measurement. Therefore, one must open the sampling bounds for $[a \ e \ i \ \Omega]^\text{T}$ to include all possible values to determine the AR unless there is a priori information regarding the uncorrelated track such as a break up or close approach relative to a stationary spacecraft. In this study, we sample from the RSO catalog (narrowed to LEO orbits) with distributions given in Fig. [2].

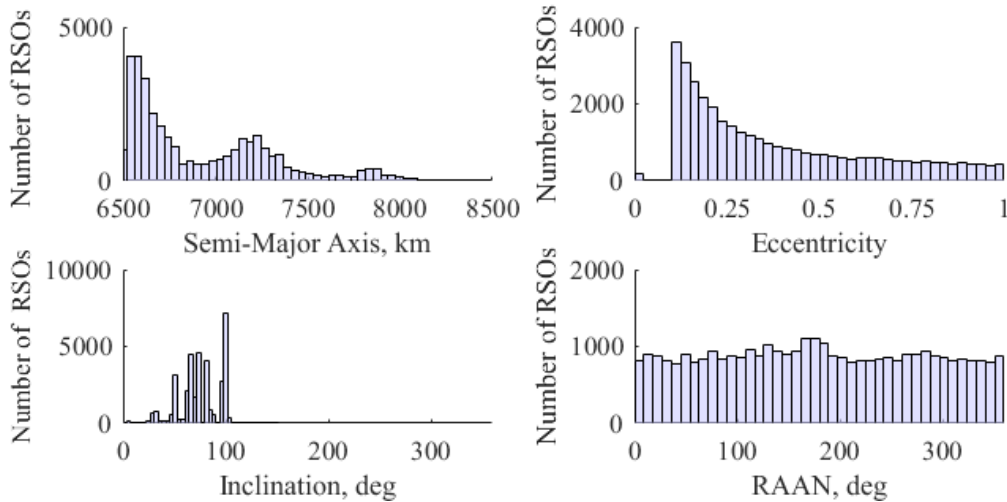


Figure 2. Distribution of the Low Earth Orbit Space Object Catalog

Evidently, according to the statistics in Figure [2] most LEO inclinations are sun synchronous while most LEO semi-major axes reside around the International Space Station (~6782 km). The object eccentricities are likely to be more circular than not while the object RAANs are uniformly distributed. Sampling from these distributions will most likely result in particle depletion—for example, given 10,000 samples of $\{y^{(j)}\} = \{\alpha^{(j)}, \delta^{(j)}, a^{(j)}, e^{(j)}, i^{(j)}, \Omega^{(j)}\}$ for

the four-dimensional PAR construction, we found that only ~250 solutions of $\{Z^{(k)}\} = \{\hat{\alpha}^{(k)}, \hat{\delta}^{(k)}, \rho^{(k)}, \hat{\rho}^{(k)}\}$ are formed for an optical measurement extract from an orbit located in the highest density region (i.e. $a = 6600$ km, $e = 0.1$, $i = 98$ deg, $\Omega \in \{0\ 360\}$ deg). As a result, we mitigate particle depletion by initially running the PAR computations on the RSO catalog distributions and then randomly resampling the resulting real particle distributions in a , e , i , and Ω without replacement to produce a denser representation of the PAR. By adopting this method, we expect a greater than four-fold increase in the number of real particles produced by the PAR.

Alternatively, to mitigate particle depletion in the proposed PAR construction, we can fit a GMM to the ensuing real solutions. The optimal number of clusters for the GMM are determined by minimizing the Akaike Information Criterion (AIC); each cluster is randomly sampled using its mean and covariance to produce a denser GMM representation of the PAR. Examples of clustering and resampling are given in Fig. [3].

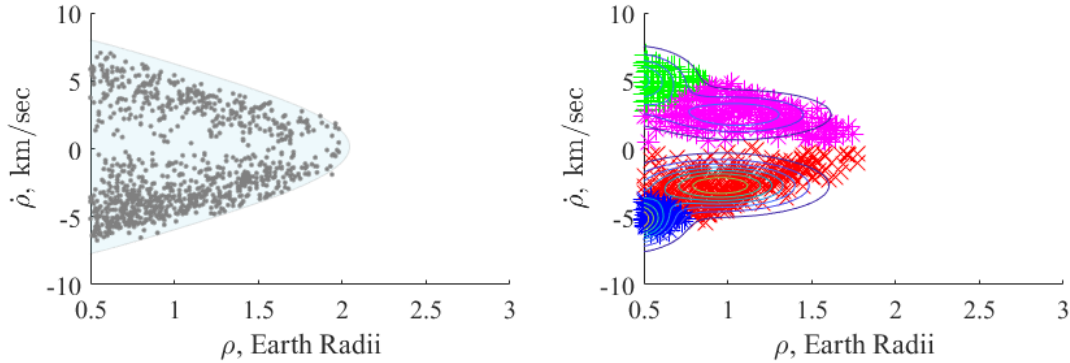


Figure 3. Example of GMM Representation of two-dimensional PAR using an AIC Clustering Optimization. The left plot shows an undersampled PAR and the right plot shows a resampled GMM PAR.

4. INITIAL ORBIT DETERMINATION USING THE CONSERVATION LAWS

Taff and Hall introduced a 4-dimensional Newton-Raphson technique (1977) that used asynchronous angles and angular rates (at t_1 and t_2) to perform an Initial Orbit Determination (IOD) using the two-body motion assumption and orbital angular momentum and energy conservation as follows,¹⁰

$$\mathbf{h}_1 = \mathbf{h}_2 \quad (14)$$

$$\epsilon_1 = \epsilon_2 \quad (15)$$

Note the subscripts ‘1’ and ‘2’ designate times t_1 and t_2 and will be used as such through the rest of this paper.

Specifically, the Taff-Hall technique solves for two two-dimensional optical attributable vectors that give four unknowns in four equations: three from Eq. [14] and one from Eq. [15]. In a later study [11], Taff et al. admitted the proposed solution did not work well.¹¹ They attempted to reduce the problem to a single dimension by setting Eq. [15] with a single unknown in ρ_2 . From there they assumed a value for ρ_2 and analytically solved for ρ_1 , $\hat{\rho}_1$, and $\hat{\rho}_2$ by using Eq. [14]. Then they plugged the results of the solved variables into $(\epsilon_1 - \epsilon_2)$, if the ensuing result was zero a root was found, otherwise they incremented ρ_2 until the sign of $(\epsilon_1 - \epsilon_2)$ changed. They decreased or increased (depending on the sign of the energy difference) the ρ_2 step-size by a factor of ten until a root was found and set their search region to $1 \text{ Earth Radii} < \rho_2 < 10 \text{ Earth Radii}$ before declaring a failure. At the time of their analysis, they asserted without a clearer and deeper understanding of the sensitivities to their method, they regarded it as a failure.

The underlying investigation in this study does not attempt to solve the initial orbit determination problem. Instead we adapt the Taff-Hall technique and update an optical PAR created at time t_1 (using the probabilistic techniques summarized in the second section) with either a radar or optical measurement obtained at time t_2 to produce an implicit-Bayesian and non-Gaussian representation of the uncertainty at the time of the second measurement. However, prior to presenting the proposed implicit-Bayesian technique we first review a common Bayesian filtering scheme in the next section for comparative purposes.

5. Bayesian Uncertainty Update Using an Ensemble Kalman Filter

The RSO tracking problem in general, is nonlinear in state dynamics and observations, making it ill-suited for linear filtering techniques such as the Kalman Filter. Extensions to the linear Kalman Filter such as an extended Kalman

Filter (EKF) or unscented Kalman Filter (UKF) are available but we wish to maintain a non-deterministic particle representation so that we can propagate the uncertainty using the true object dynamics. Alternatively, we could instead resort to a particle filtering approach by sampling from a distribution represented by a particle representation at the update step, assigning a weight to each particle, and resampling those particles with higher weights to create an updated pdf. However, weight disparity or particle depletion is common in such techniques that could lead to its collapse. As a result, this study employs Bayesian filtering (for comparative purposes) using an ensemble Kalman Filter (EnKF), a particle filter in which an artificial data matrix is used to avoid particle depletion.

We believe the EnKF lends itself well to the presentation situation since the four-dimensional PAR generated at t_1 becomes the heuristic representation of the ensemble of states updated by the filter at t_2 . Specifically, the ensemble of states is propagated through a nonlinear system to the time of the radar measurement (that contains sampling error from a normal distribution with the mean and covariance provided in the previous section) and updated by the EnKF to produce a new pdf of the particle representation. The proposed Bayesian filtering scheme is expected to produce a Gaussian representation of the uncertainty at the time of the second measurement. The authors note a Particle Gaussian Mixture (PGM) filter could be employed instead that would provide a non-Gaussian posterior; however, such a filter would require an optimal clustering algorithm, one that was not pursued as part of this study. Nonetheless, the results of the proposed implicit-Bayesian approach detailed in the previous section are compared to those using an EnKF. Gillijns et al. provide the following equations for the analysis and forecast steps in the EnKF used in this study,¹²

Analysis Step:

$$\hat{K}_k = \hat{P}_{xy_k}^f (\hat{P}_{yy_k}^f)^{-1} \quad (16)$$

$$x_k^{ai} = x_k^{fi} + \hat{K}_k \left(y_k + v_k^i - h(x_k^{fi}) \right) \quad (17)$$

$$\bar{x}_k^a = 1/q \sum_{i=1}^q x_k^{ai} \quad (18)$$

Forecast Step:

$$x_k^{fi} = f(x_k^{ai}, u_k) + \omega_k^i \quad (19)$$

$$\bar{x}_{k+1}^f = 1/q \sum_{i=1}^q x_{k+1}^{fi} \quad (20)$$

$$E_k^f = \left[x_{k+1}^{f1} - \bar{x}_{k+1}^f \dots x_{k+1}^{fq} - \bar{x}_{k+1}^f \right] \quad (21)$$

$$E_{y_k}^a = \left[y_k^{f1} - \bar{y}_k^f \dots y_k^{fq} - \bar{y}_k^f \right] \quad (22)$$

$$\hat{P}_{xy_k}^f = \frac{1}{q-1} E_k^f (E_{y_k}^f)^T, \hat{P}_{yy_k}^f = \frac{1}{q-1} E_{y_k}^f (E_{y_k}^f)^T \quad (23)$$

Note \hat{K}_k is the filter gain, $\hat{P}_{xy_k}^f$ and $\hat{P}_{yy_k}^f$ are the forecasted cross-correlated and correlated covariance matrices, x is the state estimate, \bar{x} is the ensemble mean, f is the nonlinear dynamical system, y is the observation, v is a zero-mean random variable representing noise added to the observation, h represents a mapping from the state space of x to the state space of y , q is the number of ensemble states, ω is a zero-mean random variable representing noise added to the propagation of x , E_k is the state estimate residual matrix, and E_{y_k} is the measurement residual matrix.

For our purposes, each sampled radar measurement $\{\rho_2^{(k)}, \dot{\rho}_2^{(k)}\}$ represents $y_k + v_k^i$ where y_k is given by $[\rho_2 \ \dot{\rho}_2]^T$ and v_k^i is obtained from $[\mu^\rho \ \mu^{\dot{\rho}}]^T$ and $[\Sigma^\rho \ \Sigma^{\dot{\rho}}]^T$. The function f is represented by the two-body equations of motion that provide the physics update between the two asynchronous measurements. The function h is a mapping from Cartesian to ρ - $\dot{\rho}$ space given by the following equations,

$$\rho = |\mathbf{x} - \mathbf{o}| \quad (24)$$

$$\dot{\rho} = [(\mathbf{x} - \mathbf{o}) \cdot (\mathbf{x} - \mathbf{o})] / |\mathbf{x} - \mathbf{o}| \quad (25)$$

$$\delta = \sin^{-1}(\rho_R) |\rho| \quad (26)$$

$$\alpha = \cos^{-1} \left(\rho_I / \sqrt{\rho_I^2 + \rho_J^2} \right) \quad (27)$$

Note \mathbf{o} is the inertial sensor position.

6. Implicit-Bayesian Uncertainty Update Using the Conservation Laws

In this section, we describe the proposed implicit-Bayesian technique to update a PAR with a second asynchronous and heterogeneous measurement. Specifically, we update the optical PAR at t_1 with either an optical or radar measurement at t_2 using the conservation laws. In fact, a pair of asynchronous optical and radar or optical and optical measurements produce eight unknowns in $[\rho_1, \dot{\rho}_1, \dot{\alpha}_1, \dot{\delta}_1]^T$ and $[\alpha_2, \delta_2, \dot{\alpha}_2, \dot{\delta}_2]^T$ or $[\rho_1, \dot{\rho}_1, \dot{\alpha}_1, \dot{\delta}_1]^T$ and $[\rho_2, \dot{\rho}_2, \dot{\alpha}_2, \dot{\delta}_2]^T$. Four of the unknowns are extracted from the four-dimensional PAR at t_1 in $\{Z^{(k)}\} = \{\dot{\alpha}^{(k)}, \dot{\delta}^{(k)}, \rho^{(k)}, \dot{\rho}^{(k)}\}$ for $k = 1, \dots, M$, and the resulting unknowns in $[\alpha_2, \delta_2, \dot{\alpha}_2, \dot{\delta}_2]^T$ or $[\rho_2, \dot{\rho}_2, \dot{\alpha}_2, \dot{\delta}_2]^T$ are solved using the Newton-Raphson method through the following four nonlinear equations formed by Eqs. (14) and (15),

Optical-Radar Update:

$$\mathbf{h}(\rho_1, \dot{\rho}_1) - \mathbf{h}(\dot{\alpha}_2, \dot{\delta}_2) = 0 \quad (28)$$

$$\epsilon(\rho_1, \dot{\rho}_1) - \epsilon(\dot{\alpha}_2, \dot{\delta}_2) = 0 \quad (29)$$

Optical-Optical Update:

$$\mathbf{h}(\rho_1, \dot{\rho}_1) - \mathbf{h}(\rho_2, \dot{\rho}_2) = 0 \quad (30)$$

$$\epsilon(\rho_1, \dot{\rho}_1) - \epsilon(\rho_2, \dot{\rho}_2) = 0 \quad (31)$$

Note Eqs. [28] and [30] are sets of three angular momentum equations.

Essentially, we present a procedure to map the uncertainty represented by a particle at t_1 , $p(\alpha_1, \delta_1, \dot{\alpha}_1, \dot{\delta}_1, \rho_1, \dot{\rho}_1)$, to an uncertainty at t_2 , $p(\alpha_2, \delta_2, \dot{\alpha}_2, \dot{\delta}_2, \rho_2, \dot{\rho}_2)$, by running the Newton-Raphson method on each particle generated at t_1 . Using this technique, the non-uniformity of the uncertainty is preserved through the conservation equations. Sensor noise statistics in the second asynchronous radar or optical measurement are assumed to be Gaussian with means $[\mu^{\rho_2} \ \mu^{\dot{\rho}_2}]^T$ or $[\mu^{\alpha_2} \ \mu^{\delta_2}]^T$ and covariances $[\Sigma^{\rho_2} \ \Sigma^{\dot{\rho}_2}]^T$ or $[\Sigma^{\alpha_2} \ \Sigma^{\delta_2}]^T$, respectively. Additionally, the measurement samples $\{\rho_2^{(k)}, \dot{\rho}_2^{(k)}\}$, $k = 1, \dots, M$, or $\{\alpha_2^{(k)}, \delta_2^{(k)}\}$, $k = 1, \dots, M$, are uniformly sampled from $p(\rho_2, \dot{\rho}_2)$ or $p(\alpha_2, \delta_2)$, respectively. To initialize the Newton-Raphson method, we took a quadrant-step approach in angle space. Meaning, the initial guesses for $p(\alpha_2, \delta_2)$ are eight combinations between $\alpha_2 \in \{\frac{\pi}{4}, \frac{3\pi}{4}, \frac{5\pi}{4}, \frac{7\pi}{4}\}$ and $\delta_2 \in \{\frac{\pi}{4}, \frac{3\pi}{4}\}$ for sensors in the northern hemisphere and $\alpha_2 \in \{\frac{\pi}{4}, \frac{3\pi}{4}, \frac{5\pi}{4}, \frac{7\pi}{4}\}$ and $\delta_2 \in \{\frac{5\pi}{4}, \frac{7\pi}{4}\}$ for sensors in the southern hemisphere. On the other hand, the initial guesses for $p(\rho_2, \dot{\rho}_2)$ are $\rho_2 \in \{\rho^{(1)}, \rho^{(2)}\}$ and $\dot{\rho}_2 \in \{\dot{\rho}^{(1)}, \dot{\rho}^{(2)}\}$ where we iterate on the range of $\dot{\rho}_2$ for each ρ_2 while looking for solutions that obey the conservation laws.

The initial guesses for $[\dot{\alpha}_2 \ \dot{\delta}_2]^T$ are solved for each $[\alpha_2, \delta_2]^T$ or $[\rho_2, \dot{\rho}_2]^T$ guess using the pseudo-inverse of the matrix A formulated in Eq. 12, the given optical measurement sample $\{\alpha_2^{(k)}, \delta_2^{(k)}\}$ with appropriate noise statistics, and the sampled $\{a^{(j)}\}$, $\{e^{(j)}\}$, $\{i^{(j)}\}$, and $\{\Omega^{(j)}\}$, $j = 1, \dots, N$ at t_1 that produced $\{\alpha_1^{(k)}, \delta_1^{(k)}, \dot{\alpha}_1^{(k)}, \dot{\delta}_1^{(k)}, \rho_1^{(k)}, \dot{\rho}_1^{(k)}\}$. The entire process is repeated for each k^{th} optical PAR particle and the mapping becomes $\{\alpha_1^{(k)}, \delta_1^{(k)}, \dot{\alpha}_1^{(k)}, \dot{\delta}_1^{(k)}, \rho_1^{(k)}, \dot{\rho}_1^{(k)}\}$ where, $k = 1, \dots, M$ to $\{\alpha_2^{(l)}, \delta_2^{(l)}, \dot{\alpha}_2^{(l)}, \dot{\delta}_2^{(l)}, \rho_2^{(l)}, \dot{\rho}_2^{(l)}\}$ where $l = 1, \dots, O$. Furthermore, for each root (or roots) determined at a Newton-Raphson iteration-step, the particles $\{\alpha_1^{(k)}, \delta_1^{(k)}, \dot{\alpha}_1^{(k)}, \dot{\delta}_1^{(k)}, \rho_1^{(k)}, \dot{\rho}_1^{(k)}\}$ and $\{\alpha_2^{(l)}, \delta_2^{(l)}, \dot{\alpha}_2^{(l)}, \dot{\delta}_2^{(l)}, \rho_2^{(l)}, \dot{\rho}_2^{(l)}\}$ are mapped to $\{x_1^{(k)}, y_1^{(k)}, z_1^{(k)}, \dot{x}_1^{(k)}, \dot{y}_1^{(k)}, \dot{z}_1^{(k)}\}$ and $\{x_2^{(l)}, y_2^{(l)}, z_2^{(l)}, \dot{x}_2^{(l)}, \dot{y}_2^{(l)}, \dot{z}_2^{(l)}\}$ and Eq. 13 is employed to filter out solutions where the signs of the third component of the eccentricity vectors do not match. In other words, we use the conservation in the eccentricity vector to eliminate solutions between the two measurements that have their non-planar eccentricity vector components pointed in opposite directions.

Attempts to optimize the preceding nonlinear system were pursued resulting in very minor instances of iterations that produced single roots from all quadrant-step guesses. In fact, at most 2 and 4 roots are retrieved with and without the use of the eccentricity vector constraint, respectively, which means $O \neq M$. We believe a single global solution is simply unattainable in the mapping from $\{\alpha_1^{(k)}, \delta_1^{(k)}, \dot{\alpha}_1^{(k)}, \dot{\delta}_1^{(k)}, \rho_1^{(k)}, \dot{\rho}_1^{(k)}\}$ to $\{\alpha_2^{(l)}, \delta_2^{(l)}, \dot{\alpha}_2^{(l)}, \dot{\delta}_2^{(l)}, \rho_2^{(l)}, \dot{\rho}_2^{(l)}\}$ by strictly sampling a , e , i , and Ω , as these elements are limited to the characterization of the shape and orientation of the orbit and not the location of the object within its orbital plane.

Consequently, Fig. 4 shows the uncertainty quantification of the PAR using the proposed implicit-Bayesian approach compared to the Bayesian approach using an EnKF. The top and bottom plots demonstrate asynchronous radar and optical measurement updates, respectively. The green particles represent the propagation of the PAR from t_1 to t_2 while the red particles represent the EnKF update at t_2 . Blue particles are superimposed by the Bayesian updated and propagated particles. The radar update produces a posterior shaped like a dish depicting uncertainty in the slant-range direction while the optical update produces a posterior that contains solutions across four quadrants of right ascension. As we'll see in the next section, the implicit-Bayesian posterior will remain Gaussian in Cartesian position space while non-Gaussian in Cartesian velocity space, albeit bimodally.

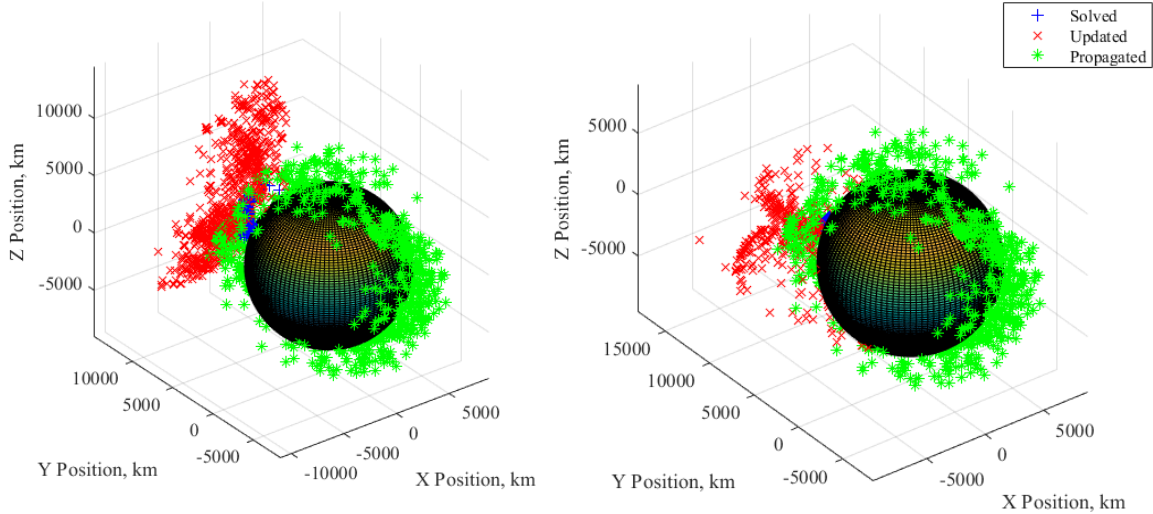


Figure 4. Examples of Implicit-Bayesian and Bayesian Uncertainty Quantification of the PAR at the time of a second asynchronous measurement. The left and right plots demonstrate an asynchronous radar measurement and optical measurement update, respectively.

7. Simulated Examples

In this section, we provide two pairs of numerical examples that demonstrate the proposed debris object initialization using the PAR with asynchronous heterogeneous measurements. Specifically, we use the implicit-Bayesian algorithm presented in this paper to provide an uncertainty representation using an optical measurement at t_1 and either a radar or optical measurement at t_2 . The measurements are sampled from a truth low Earth orbit with the parameters listed in Table 2.

Table 2. Orbital Elements of the Truth Orbit

Orbital Element	Value	Units
Semi-major axis, a (km)	7,230	km
Eccentricity, e	0.1	—
Inclination, i (deg)	98	deg
Argument of Perigee, ω (deg)	300	deg
Right Ascension of the Ascending Node, Ω (deg)	283.55	deg
Initial True Anomaly, θ (deg)	110.0	deg

The first example takes an angles-only optical measurement (of an untracked debris sampled from the truth orbit) in $[\alpha_1, \delta_1]^T$ with covariances $[\Sigma^{\alpha_1} \ \Sigma^{\delta_1}]^T$ at t_1 , at t_1 , develops a four-dimensional optical particle representation of the uncertainty, and then updates it 16 hours later with a radar measurement in $[\rho_2 \ \dot{\rho}_2]^T$ with covariances $[\Sigma^{\rho_2} \ \Sigma^{\dot{\rho}_2}]^T$. The second simulation takes the same four-dimensional particle cloud and updates it with an optical measurement in $[\hat{\alpha}_2 \ \hat{\delta}_2]^T$ with covariances $[\Sigma^{\hat{\alpha}_2} \ \Sigma^{\hat{\delta}_2}]^T$. Characteristics for the sensors that collect both measurements as well as the measurements themselves are presented in Table 3.

Table 3. Sensor and simulated measurement characteristics.

Input	Value	Units
\mathbf{o}_{t_1}	$[1243, -5158, 3528]^T$	km
$\dot{\mathbf{o}}_{t_1}$	$[0.376, 0.0902, -0.00054]^T$	km/s
\mathbf{o}_{t_2}	$[-2478, 5431, 2246]^T$	km
$\dot{\mathbf{o}}_{t_2}$	$[-0.396, -0.181, 0.00056]^T$	km/s
$[\mu^{\alpha_1} \ \mu^{\delta_1}]^T$	$[159.0925 \ 65.420]^T$	deg
$[\mu^{\rho_2} \ \mu^{\dot{\rho}_2}]^T$	$[2.843 \times 10^4 \ 5.297]^T$	km, km/s
$[\mu^{\alpha_2} \ \mu^{\delta_2}]^T$	$[70.469 \ -44.735]^T$	deg
$[\sigma^\alpha \ \sigma^\delta]^T$	$[2.0 \ 2.0]^T$	arc-sec
$[\sigma^\rho \ \sigma^{\dot{\rho}}]^T$	$[30 \ 3.0]^T$	cm, cm/s

For the four-dimensional PAR in both examples, the sampled set of $\{\alpha^{(j)}, e^{(j)}, i^{(j)}, \Omega^{(j)}\}, j = 1, \dots, N$ is randomly selected without replacement from the RSO LEO Catalog (downloaded on 2 May 2017) with bounds specified in Table 4. Both simulations are performed on a Dell Precision 5510 laptop with an Intel® Xeon® CPU E3-1505M v5 @ 2.80 GHz processor and 32.0 GB installed memory.

Table 4. Orbital element distribution limits.

Orbital Element	Min Value	Max Value	Units
a	6,500	8,499	km
e	0	0.999	-
i	0.173	151	deg
Ω	0.0053	360	deg

The initial run of the four-dimensional angles-only PAR was built using 10,000 samples of $\{\mathbf{y}^{(j)}\} = \{\alpha^{(j)}, \delta^{(j)}, a^{(j)}, e^{(j)}, i^{(j)}, \Omega^{(j)}\}$ and produced only 304 real particles. The uncertainty projections onto the slant-range and angle-rate planes are shown in Fig. [5]. As expected, real particles are non-uniformly distributed, albeit symmetrically, about zero. Specifically, given a true uncorrelated track, the direction of motion of the object to an observer is ambiguous; that is, the object could be ascending or descending in its orbit. Fig. [6] shows distributions in a , e , i , and Ω that formed all real particles and that support the behavior of the particles in Fig. [5]. Remarkably, we see the distributions change from the original sampling distributions in Figure [2]; specifically, a and Ω have become bimodal signaling two possible candidates for the truth orbit—an attribute that can easily be alleviated with a measurement update to a sequential Bayesian estimator or MHF. Additionally, the bimodal RAAN distribution supports the claim regarding the ascending or descending nature of the object within its orbit. In fact, we have narrowed down the likelihood of the RAAN to be two specific values that are 180 degrees apart.

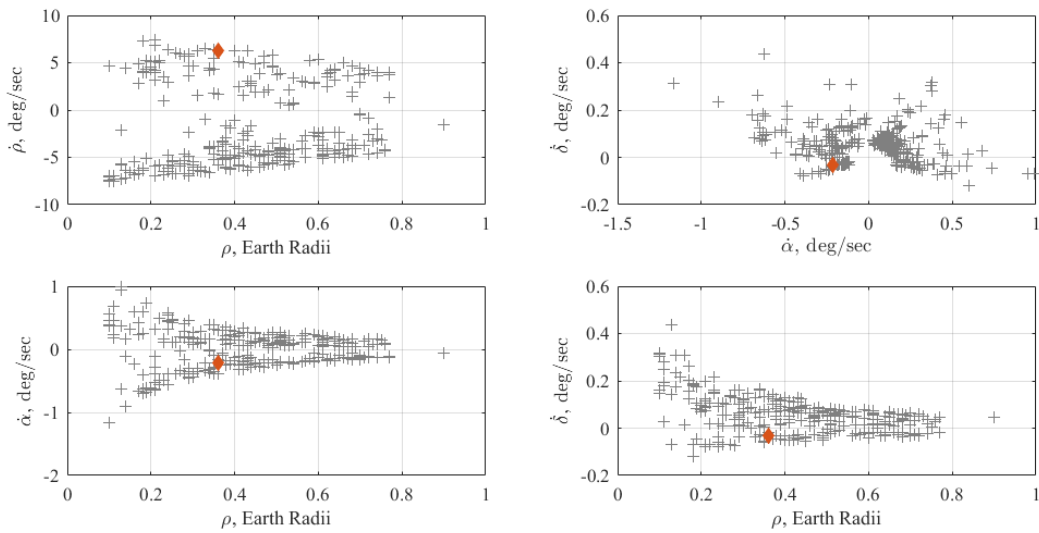


Figure 5. Four-dimensional PAR at t_1 in $\rho\dot{\rho}$, $\rho\dot{\alpha}$, $\rho\dot{\delta}$, and $\dot{\alpha}\dot{\delta}$ spaces with 304 particles. As expected, both slant-range and angular rates are undetermined in sign for a single angles-only observation. The red diamond represents the truth orbit.

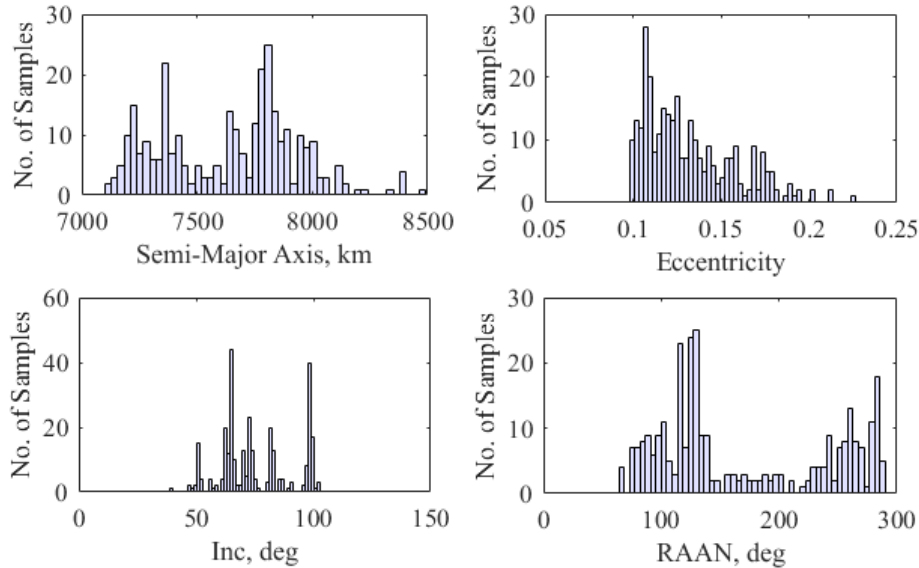


Figure 6. Orbital Element Distributions that Produced Real Particles for the four-Dimensional optical PAR at t_1 .

Next, we look at the Cartesian position and velocity distributions of the PAR particles at t_1 in Figs. [7] and [8] for reference (relative to their ensuing Bayesian and Implicit-Bayesian updates). All positions are relatively Gaussian while the velocities are clearly non-Gaussian. Again, the velocity and angle/range rates all support the ambiguity of the motion of the object within its orbit—the authors believe that by sampling solely a , e , i , and Ω , the true uncertainty of the untrack debris appears to be present in ω and θ . Perhaps, if one were to reformulate Eq. [6] in terms of equinoctial orbital elements and sample four elements in equinoctial space (that represent five Keplerian orbital elements), this could alleviate the uncertainty in the location of the object within its orbital plane. Fig. [9] provides the optical PAR after resampling without replacement that produces 1,053 real particles. Its distributions are like those depicted in Fig. [5] but with a denser representation of the PAR. Finally, Fig. [10] displays the orbital elements that produced the resampled PAR; high eccentricities with lower semi-major axes are incompatible as their trajectories

intersect the Earth while two clusters of sun synchronous inclination have RAAN values that are clearly separated by 180 degrees.

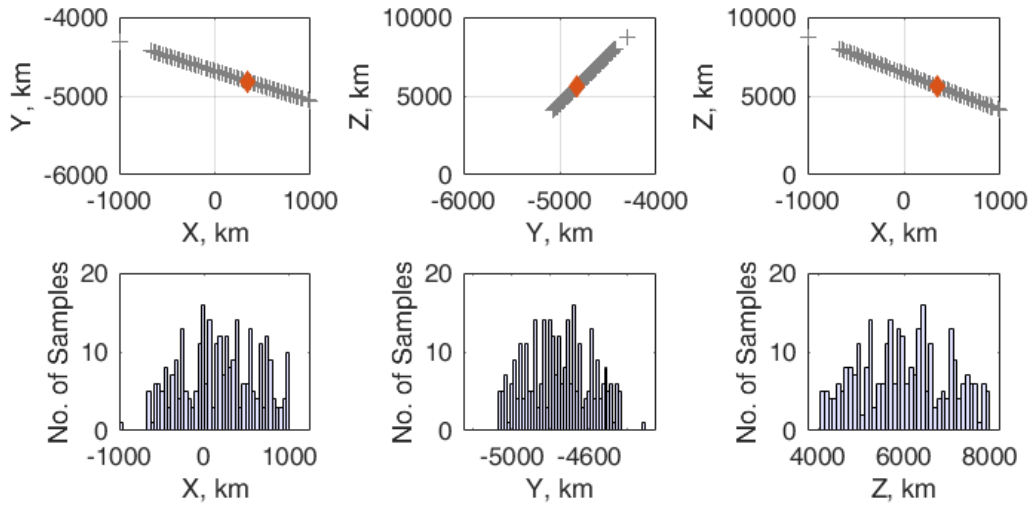


Figure 7. Cartesian Position Distributions of the Four-Dimensional Optical PAR at t_1 (Inertial Reference Frame). The red diamond represents the truth orbit.

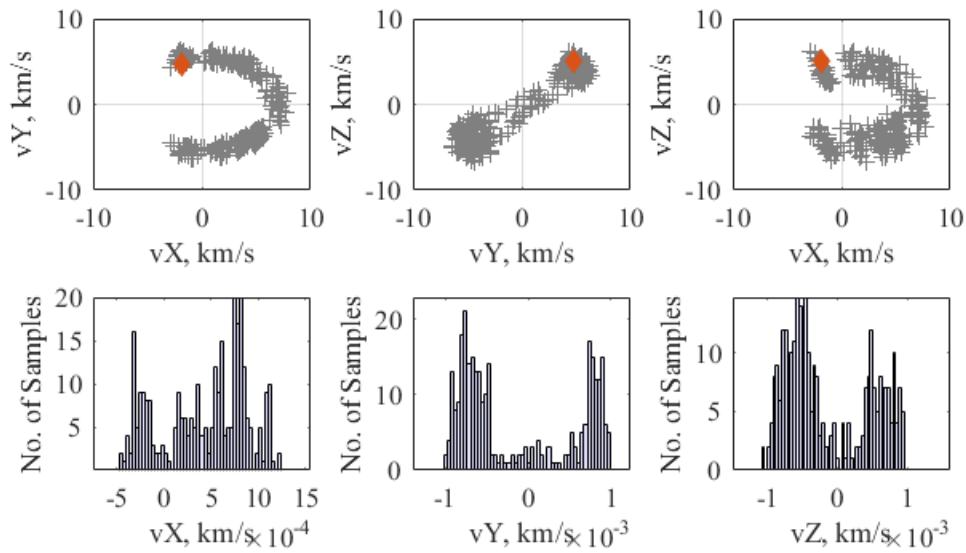


Figure 8. Cartesian Velocity Distributions of the Four-Dimensional Optical PAR at t_1 (Inertial Reference Frame). The red diamond represents the truth orbit.

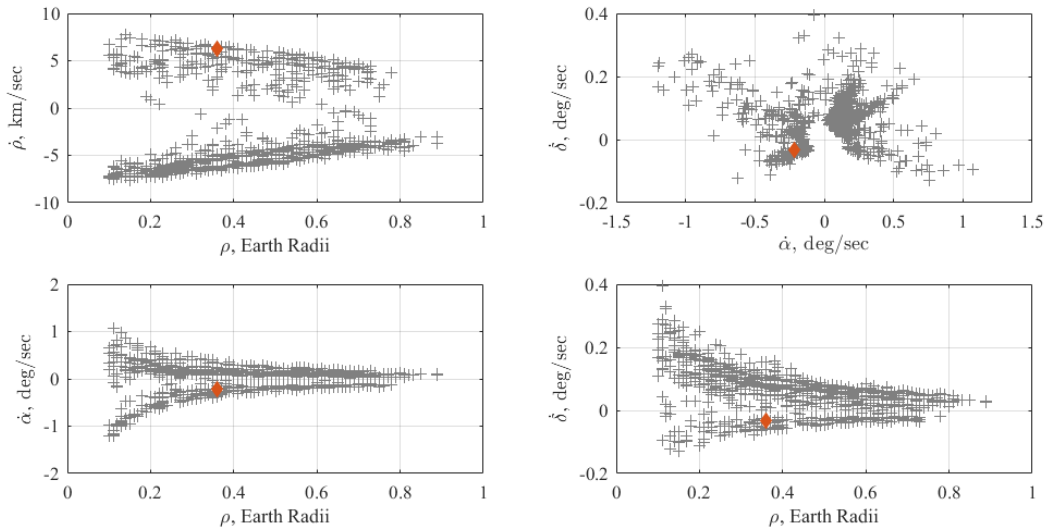


Figure 9. Four-dimensional optical PAR at t_1 in $\rho\dot{\rho}$, $\rho\dot{\alpha}$, $\rho\dot{\delta}$, and $\dot{\alpha}\dot{\delta}$ spaces with 1,053 particles demonstrating successful resampling of the orbit elements distributions in Fig. [5]. The red diamond represents the truth orbit.

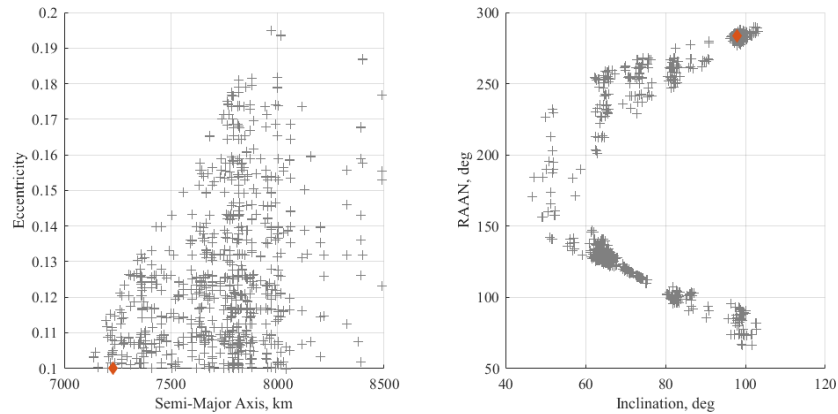


Figure 10. Four-dimensional PAR at t_1 in $a-e$ and $i-\Omega$ spaces with 1,053 particles demonstrating successful resampling of the orbit elements distributions in Fig. [5]. The red diamond represents the truth orbit.

The asynchronous optical measurement update to optical PAR at t_1 is given in Figs. [11] through [15]. Once again, we observe particle depletion in that only 166 real particles are formed in the update by using 1,053 samples from the optical PAR at t_1 —we could mitigate depletion by resampling or by applying a GMM using the techniques presented earlier. Additionally, Fig. [11] shows the optical measurement update reduces the bimodality of the slant-range-range distribution and the true orbit resides in the denser region of the particle cloud update. Next, in Fig. [12] we compare the Implicit-Bayesian and Bayesian updates using the optical measurement at t_2 . In Reference 6, we used very strict bounds when sampling i and Ω which impacted the probabilistic direction of velocity and ultimately restricted the PAR to real solutions that are either ascending or descending in their orbital plane. As a result, the prior pdf obtained using two-body propagation at t_2 (for an orbit sampled from the MEO region) was relatively small; this allowed us to successfully employ the EnKF to produce a posterior pdf such that it collapsed over the true measurement. In our present situation, since the sampling bounds of i and Ω are much larger, the prior pdf at t_2 is very large—sampling from the catalog RAAN distribution produced a non-Gaussian representation of the velocity uncertainties at t_1 (as demonstrated in Fig. [8]) that is spread between positive and negative velocities meaning to an observer on Earth, the uncorrelated, untracked debris could be moving East to West or West to East. Accordingly,

propagating the larger non-Gaussian velocity pdf to t_2 impacted the Bayesian measurement update such that the posterior did not collapse over the true measurement.

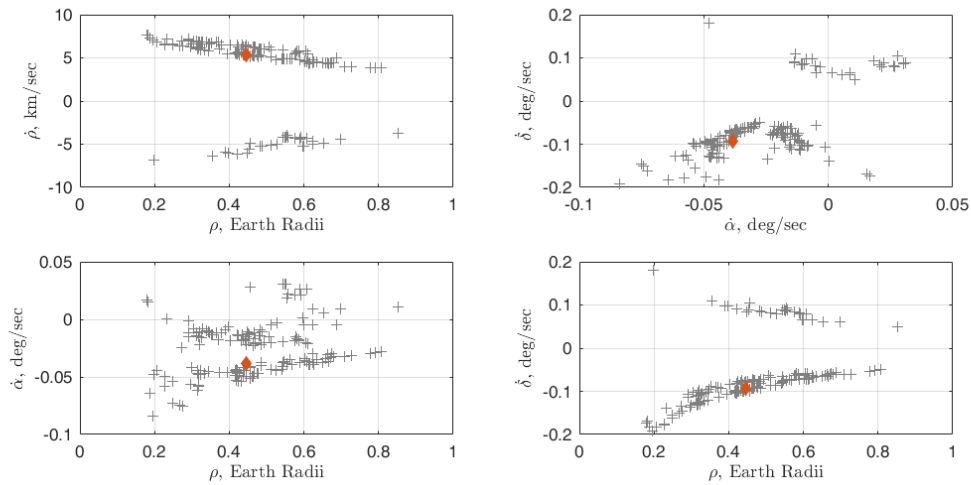


Figure 11. Implicit-Bayesian update of the four-dimensional optical PAR at t_2 in $\rho\dot{\rho}$, $\rho\dot{\alpha}$, $\rho\dot{\delta}$, and $\dot{\alpha}\dot{\delta}$ spaces using an optical measurement. 166 real particles were formed in the update. The red diamond represents the truth orbit.

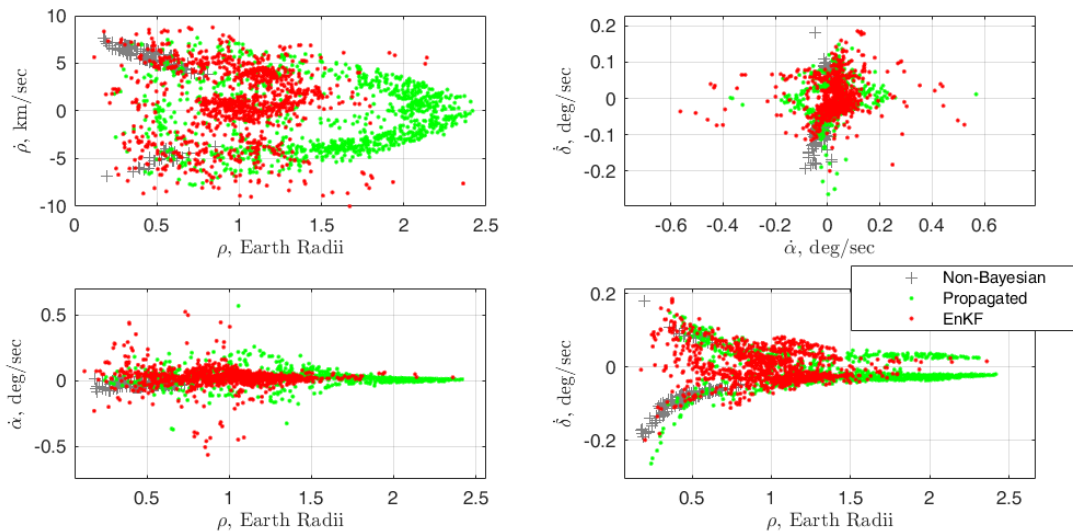


Figure 12. Comparison of Implicit-Bayesian, Propagated, and Bayesian (EnKF) updates of the four-dimensional optical PAR at t_2 in $\rho\dot{\rho}$, $\rho\dot{\alpha}$, $\rho\dot{\delta}$, and $\dot{\alpha}\dot{\delta}$ spaces using an optical measurement. 166 real particles were formed in the update. The Propagated and Bayesian solutions are superimposed over the Implicit-Bayesian solution from Fig. [11].

The differences in the velocity and RAAN distributions between Figs. [8] & [15] and [10] & [13], respectively, show the advantage of using the probabilistic admissible region—we have successfully updated an extremely non-Gaussian pdf (in Cartesian velocity space) in low Earth orbit after 16 hours of propagation to produce bimodal distributions. These distributions can be clustered and propagated forward to be used to initialize a sequential Bayesian estimator at the time of a future measurement. That is, for very poorly tracked objects, we propose a base search-space for a second asynchronous optical sensor that is tied to the conservation laws.

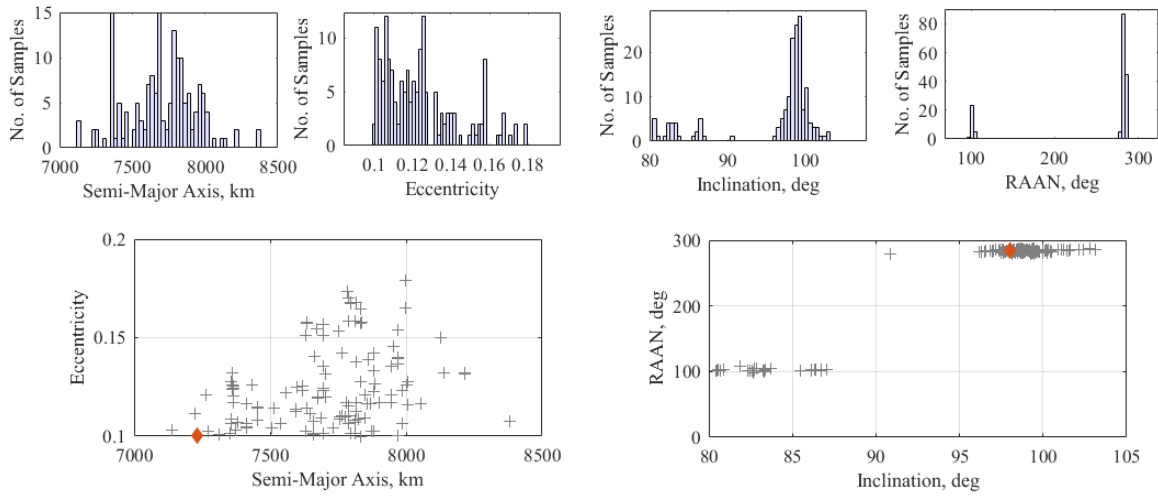


Figure 13. Orbital Element Distributions of the Implicit-Bayesian four-dimensional optical PAR update at t_2 using an optical measurement. 166 real particles were formed in the update. The red diamond represents the truth orbit.

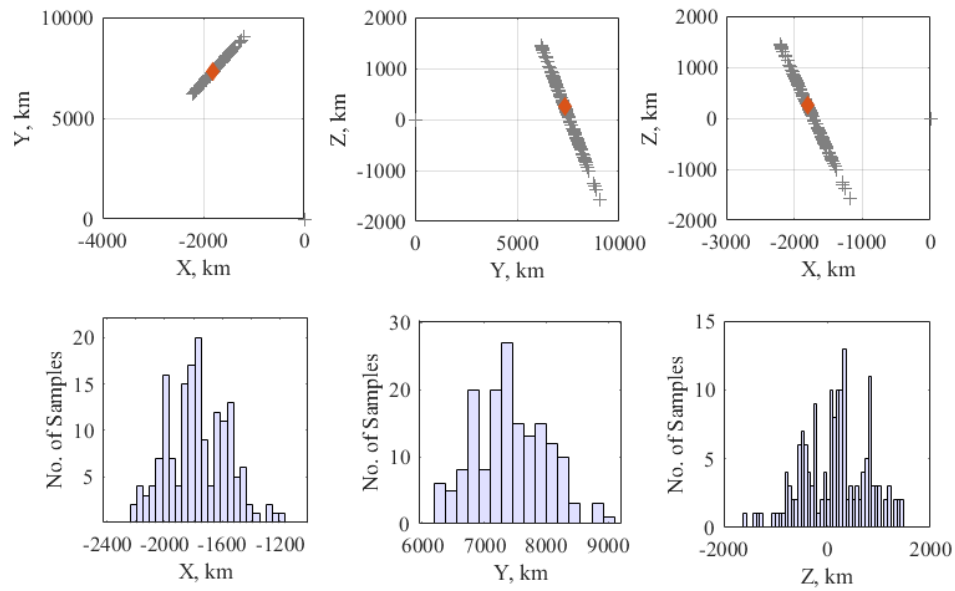


Figure 14. Cartesian Position Distributions of the Implicit-Bayesian four-dimensional optical PAR update at t_1 using an optical measurement. 166 real particles were formed in the update. The red diamond represents the truth orbit.

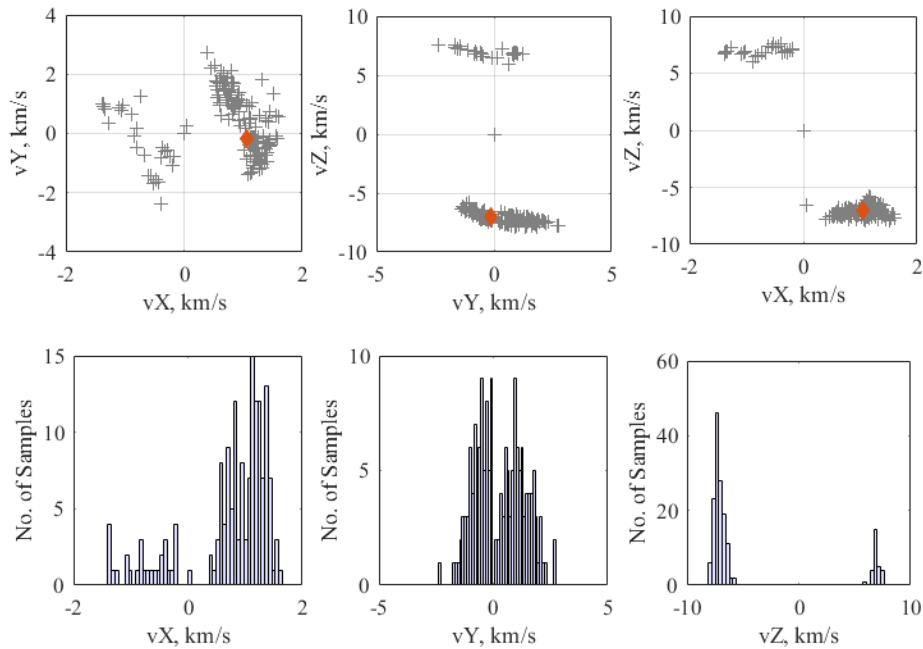


Figure 15. Cartesian Velocity Distributions of the Implicit-Bayesian four-dimensional optical PAR update at t_2 using an optical measurement. 166 real particles were formed in the update. The red diamond represents the truth orbit.

The asynchronous radar measurement update to the optical PAR at t_1 is given in Figs. [16] through [20]. This time particle depletion resulted in 373 real particles using 1,053 samples from the optical PAR at t_1 . Fig. [16] shows the radar measurement update produces a trimodal distribution in right ascension-declination space with the true orbit lying inside one cluster of particles—the distribution can easily be clustered and propagated forward using a GMM to the time of a third measurement. Next, in Fig. [17] we compare the Implicit-Bayesian and Bayesian updates using the radar measurement at t_2 as we did with the radar measurement. Again, the EnKF is unable to produce a posterior that completely collapses over the true measurement.

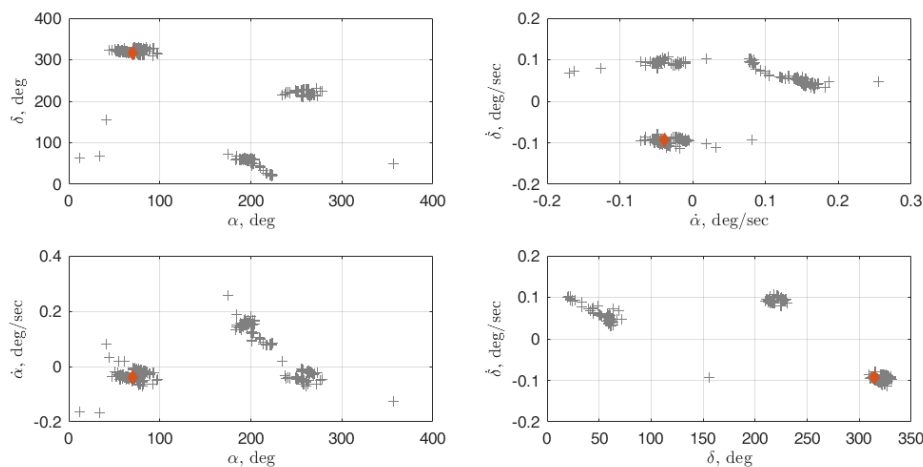


Figure 16. Implicit-Bayesian update of the four-dimensional optical PAR at t_2 $\rho\hat{\rho}$, $\rho\hat{\alpha}$, $\rho\hat{\delta}$, and $\hat{\alpha}\hat{\delta}$ spaces using a radar measurement. 373 real particles were formed in the update. The red diamond represents the truth orbit.

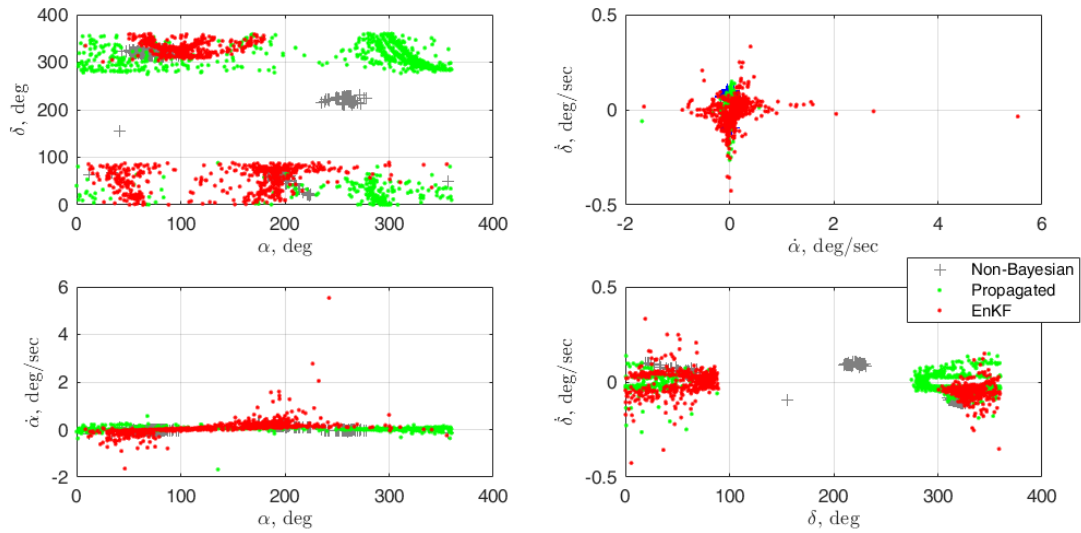


Figure 17. Comparison of Implicit-Bayesian, Propagated, and Bayesian (EnKF) update of the four-dimensional PAR at t_2 $\rho\hat{\rho}$, $\rho\hat{\alpha}$, $\rho\hat{\delta}$, and $\hat{\alpha}\hat{\delta}$ spaces using a radar measurement.

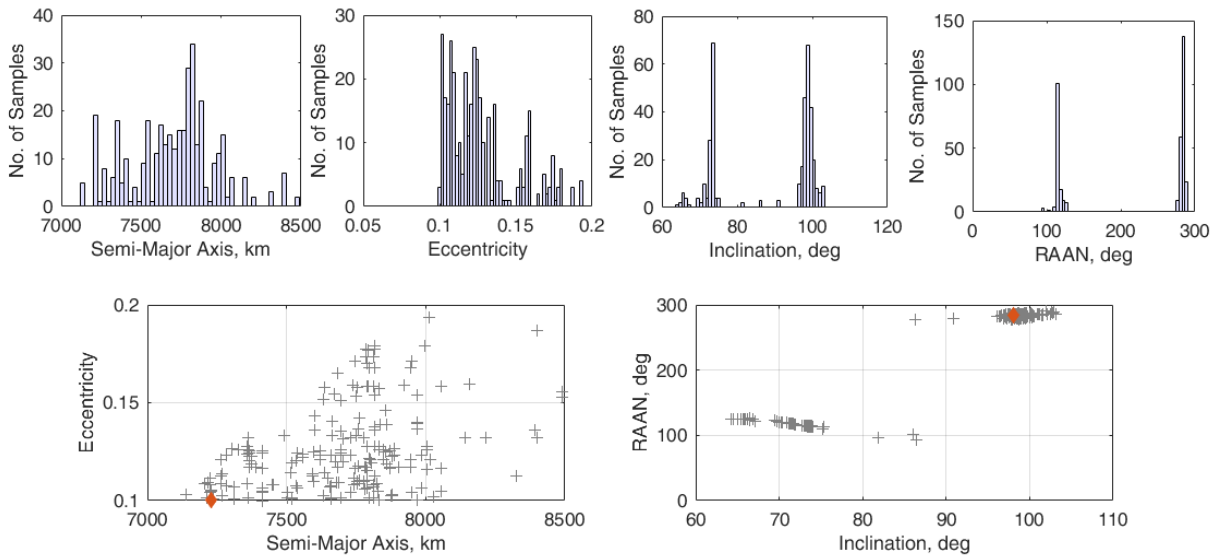


Figure 18. Orbital Element Distributions of the Implicit-Bayesian four-dimensional PAR update at t_2 using a radar measurement.

Orbital element distributions using a radar update in Fig. [18] are behaving like that were produced by the optical measurement update in Fig. [13]. The posterior has converged bimodally in i - Ω space while the distributions in a begins to shift away from its highest intensity in the catalog (~ 6250 km). Finally, comparing the optical and radar measurement updates in Cartesian y - z coordinates (Figs. [14] and [19]) demonstrates the spread of the uncertainty in two ways—radially outward from the observer’s point-of-view for the optical measurement and along the circumference of the probable orbits belonging to the radar measurement.

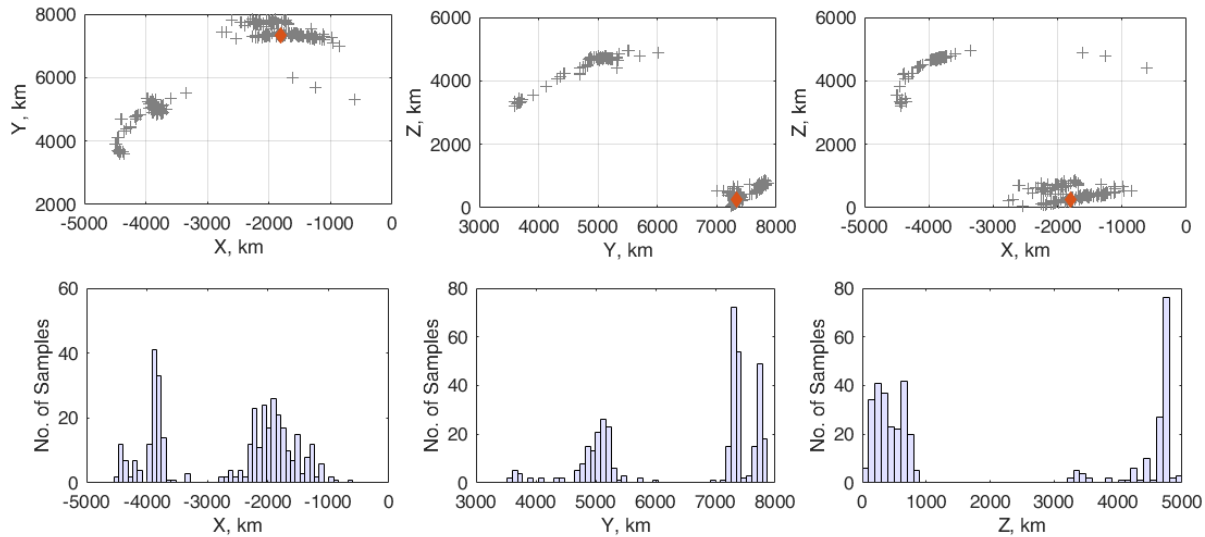


Figure 19. Cartesian Position Distributions of the Implicit-Bayesian four-dimensional PAR update at t_2 using a radar measurement.

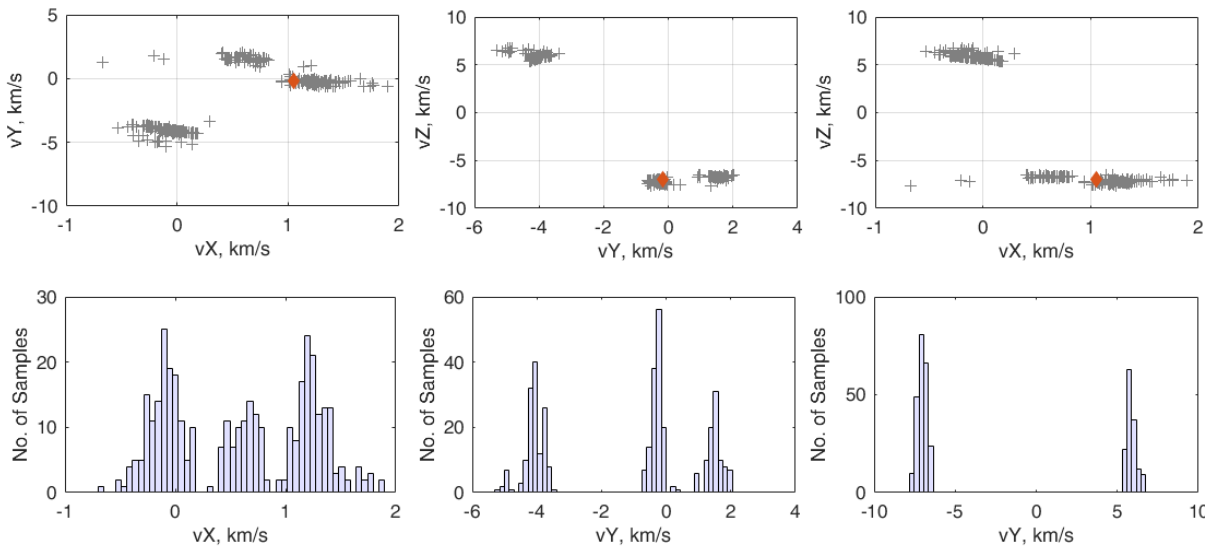


Figure 20. Cartesian Velocity Distributions of the Implicit-Bayesian four-dimensional PAR update at t_2 using a radar measurement.

8. CONCLUSION

Given an untracked and uncorrelated angles-only measurement of a piece of debris, the study in this paper seeks to sample the entire RSO catalog (for a , e , i , and Ω) to generate an optical probabilistic admissible region using a four-dimensional probabilistic technique and then to update the pdf with an asynchronous heterogeneous optical or radar measurement using the conservation of energy and conservation angular momentum. We demonstrate the successful sampling of the entire RSO catalog by showing distributions in all four orbital elements begin to collapse around the true orbit, albeit by resampling the initial orbit element PAR solutions without replacement. Furthermore, we have shown traditional Bayesian filtering is unsuitable for updating the optical PAR with an asynchronous optical or radar measurement as the posterior does not collapse over the true observation. Finally, we show the implicit-Bayesian approach produces uncertainty distributions in Cartesian space that able themselves to be clustered to form a GMM that in turn can be propagated to initialize a sequential Bayesian filter at the time of a third measurement.

Appendix

All constants used in this paper are defined here,

$$\omega_0 = |\mathbf{o}|^2 \quad (32)$$

$$\omega_1 = 2(\dot{\mathbf{o}} \cdot \mathbf{u}_\rho) \quad (32)$$

$$\omega_2 = \dot{\alpha}^2 \cos^2 \delta + \dot{\delta}^2 \quad (34)$$

$$\omega_3 = 2\dot{\alpha} \cos \delta (\dot{\mathbf{o}} \cdot \mathbf{u}_\alpha) + 2\dot{\delta} (\dot{\mathbf{o}} \cdot \mathbf{u}_\delta) \quad (35)$$

$$\omega_4 = |\dot{\mathbf{o}}|^2 \quad (36)$$

$$\omega_5 = 2(\mathbf{o} \cdot \mathbf{u}_\rho) \quad (37)$$

$$\mathbf{h}_1 = \mathbf{o} \times \mathbf{u}_\rho \quad (38)$$

$$\mathbf{h}_2 = \mathbf{u}_\rho \times (\dot{\alpha} \cos \delta \mathbf{u}_\alpha + \dot{\delta} \mathbf{u}_\delta) \quad (39)$$

$$\mathbf{h}_3 = \mathbf{u}_\rho \times \dot{\mathbf{o}} + \mathbf{o} \times (\dot{\alpha} \cos \delta \mathbf{u}_\alpha + \dot{\delta} \mathbf{u}_\delta) \quad (40)$$

$$\mathbf{h}_4 = \mathbf{o} \times \dot{\mathbf{o}} \quad (41)$$

$$c_0 = |\mathbf{h}_1|^2 \quad (42)$$

$$c_1 = 2(\mathbf{h}_1 \cdot \mathbf{h}_2) \quad (43)$$

$$c_2 = 2(\mathbf{h}_1 \cdot \mathbf{h}_3) \quad (44)$$

$$c_3 = 2(\mathbf{h}_1 \cdot \mathbf{h}_4) \quad (45)$$

$$c_4 = |\mathbf{h}_2|^2 \quad (46)$$

$$c_5 = 2(\mathbf{h}_2 \cdot \mathbf{h}_3) \quad (47)$$

$$c_6 = 2(\mathbf{h}_2 \cdot \mathbf{h}_4) + |\mathbf{h}_3|^2 \quad (48)$$

$$c_7 = 2(\mathbf{h}_3 \cdot \mathbf{h}_4) \quad (49)$$

$$c_8 = |\mathbf{h}_4|^2 \quad (50)$$

$$F = \omega_2 \rho^2 + \omega_3 \rho + \omega_4 - \frac{2\mu}{\sqrt{\rho^2 + \omega_5 \rho + \omega_0}} \quad (51)$$

$$P = c_1 \rho^2 + c_2 \rho + c_3 \quad (52)$$

$$U = c_4 \rho^4 + c_5 \rho^3 + c_6 \rho^2 + c_7 \rho + c_8 \quad (53)$$

$$a_0 = FU + \mu^2(1 - e^2) \quad (54)$$

$$a_1 = FP + \omega_1 U \quad (55)$$

$$a_2 = U + c_0 F + \omega_1 P \quad (56)$$

$$a_3 = P + c_0 \omega_1 \quad (57)$$

$$a_4 = c_0 \quad (58)$$

Note \mathbf{r} and $\dot{\mathbf{r}}$ are defined as follows,

$$\mathbf{r} = \mathbf{o} + \rho \mathbf{u}_\rho \quad (59)$$

$$\dot{\mathbf{r}} = \dot{\mathbf{o}} + \dot{\rho} \mathbf{u}_\rho + \rho \dot{\alpha} \cos \delta \mathbf{u}_\alpha + \rho \dot{\delta} \mathbf{u}_\delta \quad (60)$$

References

- ¹ Hill, K., Sabol, C., and Alfriend, K. T., "Comparison of Covariance-Based Track Association Approaches Using Simulated Radar Data," *AAS Journal of the Astronautical Sciences*, Vol. 59, Nos. 1 & 2, Jan-June 2012, pp. 287-306.
- ² I. I. Hussein, W. H. Zaidi, W. R. Faber, C. W. T. Roscoe, M. P. Wilkins, J. Paul W. Schumacher, and M. Bolden, "A Randomized Sampling Based Approach to Multi-Object Tracking with Comparison to HOMHT." *Proceedings of the AAS/AIAA Space Flight Mechanics Meeting*, San Antonio, TX, February 5-9, 2017. Paper AAS 17-415.
- ³ P. W. Schumacher, Jr., M. P. Wilkins, and C. W. T. Roscoe, "Parallel Algorithm for Track Initiation for Optical Space Surveillance." *Proceedings of the 6th European Conference on Space Debris*, European Space Operations Center, Darmstadt, Germany, April 22-25, 2013.

- ⁴C. W. T. Roscoe, P. W. Schumacher, Jr., and M. P. Wilkins, "Parallel Track Initiation for Optical Space Surveillance using Range and Range-Rate Bounds." *Advances in the Astronautical Sciences*, Vol. 150, 2014, pp. 989-1008.
- ⁵I. I. Hussein, C. W. T. Roscoe, M. P. Wilkins, and P. W. Schumacher, Jr., "Probabilistic Admissibility in Angles-Only Initial Orbit Determination." *Proceedings of the 24th International Symposium on Space Flight Dynamics*, Laurel, MD, May 5-9, 2014.
- ⁶W. H. Zaidi, W. R. Faber, I. I. Hussein, M. Mercurio, C. W. T. Roscoe, M. P. Wilkins, and P. W. Schumacher Jr., "Debris Object Orbit Initialization Using the Probabilistic Admissible Region with Asynchronous Heterogeneous Measurements." *Proceedings of the AAS/AIAA Astrodynamics Specialist Conference*, Stevenson, WA, August 21-24, 2017, Pre-Print AAS 17-592.
- ⁷R.E. Kalman, "A new approach to linear Filtering and prediction problems." *Transaction of the ASME –Journal of Basic Engineering*, 82 (Series D), 1960, pp. 35–45.
- ⁸S. Julier and J. Uhlmann, "Unscented filtering and nonlinear estimation." *Proceedings of the IEEE*, Vol. 92, No. 3, 2004, pp. 401–422.
- ⁹D. Farnocchia, G. Tommei, A. Milani, and A. Rossi, "Innovative Methods of Correlation and Orbit Determination for Space Debris." *Celestial Mechanics and Dynamical Astronomy*, Vol. 107, 2010, pp. 169–185.
- ¹⁰L.G. Taff, and D.L. Hall, *Celestial Mechanics*. Vol. 16, Issue 4, 1977, pp. 481-488.
- ¹¹L.G. Taff, P. M. S. Randall, and S. A. Stansfield, "Angles-Only, Ground-Based, Initial Orbit Determination." *Massachusetts Institute of Technology Lincoln Laboratory*, Report No. 618, July 13, 1984.
- ¹²S. Gillijns et. al., "What Is the Ensemble Kalman Filter and How Well Does It Work?" *Proceedings of the 2006 American Control Conference*, Minneapolis, Minnesota, USA, June 14-16, 2006, pp 4448-4453.